Available online at www.sciencedirect.com

jmr&t Journal of Materials Research and Technology

www.jmrt.com.br

Original Article

Electrical and magnetic properties of $NiTiO_3$ nanoparticles synthesized by the sol–gel synthesis method and microwave sintering

Pavithra C.[a,*], *Madhuri W.*[a,b]

[a] *Center for Crystal Growth, VIT University, Vellore, Tamil Nadu 632 014, India*
[b] *Leibniz Institute for Solid State and Materials Research, Dresden 01069, Germany*

ARTICLE INFO

Article history:
Received 24 August 2016
Accepted 26 July 2017
Available online 29 May 2019

Keywords:
$NiTiO_3$
X-ray diffraction
HRSEM
Impedance analysis
M–H curve

ABSTRACT

In this paper, we focused on microwave sintered $NiTiO_3$ nanoparticles synthesized via sol–gel method. The crystal structure was determined by the X-ray diffraction. Vibrational bands related to Ni–O and Ti–O bands were confirmed using the Fourier transform infrared spectrum. These $NiTiO_3$ ceramics obeyed semiconductor behavior of Arrhenius type. The activation energy was found to be 0.04 μeV. The M–H curve exhibited superparamagnetic behavior at room temperature.

1. Introduction

Inorganic materials especially in lead titanate, barium titanate, strontium titanate, cobalt titanate and nickel titanate have wide applications in electronic industry. These are piezoelectric in nature. A few of them can exhibit an antiferromagnetism [1]. Metal oxide nanoparticles are important to develop advanced catalyst and sensory materials [2]. Titanium based perovskite $ATiO_3$ (A = Pb, Ba, Sr, Zn and Ni) are widely used in photoemission and photocatalysis. $NiTiO_3$ is used as an photocatalyst in the removal of organic pollutants from gas sensitivity [3]. $NiTiO_3$ is an n-type semiconductor with wide-spread usage [4]. At room temperature, it exhibits antiferromagnetism due to order–disorder transition between Ni and Ti which is also responsible for high curie transition temperature, $T_c = 1570$ [5].

Different methods are successfully synthesized the $NiTiO_3$ such as, solid state, hydrothermal, molten salt, polymeric precursor, electrospinning and a sol–gel method. Electrospinning method yielded good results in X-ray diffraction at 600 °C calcination temperature though there is no addition TiO_2 was present. Of all synthesis methods, sol–gel technique is easy to process, having homogenate and controlled reaction [6–12]. The work objective is to synthesize $NiTiO_3$ nano-particles by sol–gel and then process by sintering, this is the first time to report the microwave sintered $NiTiO_3$ ceramics. Compared to conventional sintering, microwave sintering consumes less energy and time. The ceramics sintered in

* *Corresponding author.*
E-mail: madhuriw12@hotmail.com (P. C.).
https://doi.org/10.1016/j.jmrt.2017.07.007

microwaves have exhibited high density, uniform grain growth and homogeneous [13–15]. Therefore, in this paper, we present how $NiTiO_3$ nanoparticles are obtained by the sol–gel synthesis, microwave processing and its structural, microstructural, electrical and magnetic characterization.

2. Experimental details

2.1. *Sol–gel synthesis of $NiTiO_3$ nanoparticles*

Initially, analytical grade nickel nitrate [Sigma-Aldrich, 97.0%, $Ni(NO_3)_2{\cdot}6H_2O$] and titanium(IV) butoxide [Sigma-Aldrich, 97.0%, $Ti(OC_4H_9)_4$] are taken in a stoichiometric ratio. Then nickel nitrate is dissolved in 16.88 ml of glacial acetic acid under continuous stirring. This mixed solution is dehydrated at 100 °C for 20 min and is cooled to room temperature. Then, titanium (IV) butoxide is added very slowly under constant stirring for 45 min at room temperature. Next, the mixture of ethanol and water are added drop by drop to prevent fast gelation. Then the gel is heated at 100 °C in an oven to obtain nanoparticles. Further, the prepared powder is calcined at 730 °C for 45 min at the rate of 30 °C per min in a microwave furnace. The green sample is grinded using agate mortar for 6 h. Finally, the powder is pressed into pellet and densification is done at 1000 °C for 45 min at the rate of 30 °C per min in a microwave furnace.

2.2. *Characterizations*

X-ray diffraction is carried out using powder X-ray instrument (Bruker D8) with Cu Kα radiation (1.5406 Å). FT-IR is recorded using Siemens Instrument. The surface morphological and compositional analyses were studied using high resolution scanning electron microscope (FEI Quanta FEG 200) and energy dispersive X-ray spectrometer (EDX). Conductivity and impedance spectroscopy of nickel titanate are carried out using the LCR Hi TESTER (HIOKI-3532-50). The sample is placed between the electrodes of the computer interfaced oven. The magnetic properties of nickel titanate are studied by VSM instrument (LAKESHORE-7407).

3. Results and discussion

3.1. *Structural and microstructural characterization*

Fig. 1 shows the X-ray diffraction pattern of $NiTiO_3$. All the peaks of X-ray diffraction pattern are matching with JCPDS file no 83-0198 and [5]. The appearance of the small additional TiO_2 rutile phase peak is represented by * which is also confirmed in the JCPDS file no 87-1165. Approximately 15% of rutile phase is estimated by Reitvelds analysis. The rutile phase is more stable than anatase phase at a high temperature [16]. These peaks represent rhombohedral crystal structure and R3 space group. The lattice parameters are evaluated using the powder X software and are found to be $a = b = 5.03$ Å and $c = 13.79$ Å. The volume of the unit cell is found to be 348 Å^3, these values match with those in Ref. [5]. Density (according to Archimedes principle) and porosity are estimated using

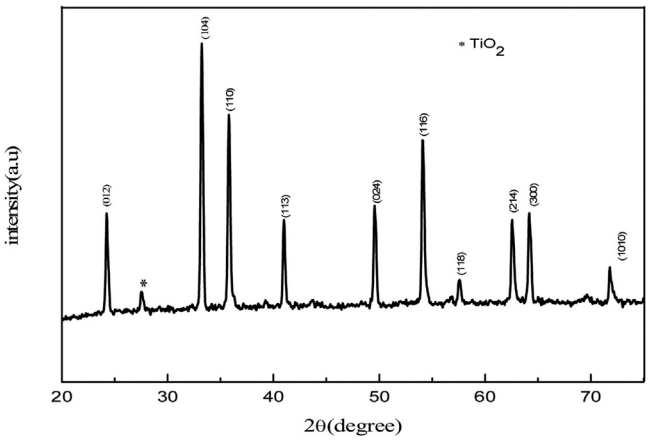

Fig. 1 – X-ray diffraction of $NiTiO_3$.

relation (1) and (2). The values are to be 5.046 g/cm^3 and 0.143. The theoretical density (from X-ray studies) is found using the relation (3) the value is 5.89 g/cm^3.

$$\rho_B = \frac{m_{air}}{m_{air} - m_{xylens}} \times \rho_{xylens} \quad (1)$$

$$P = 1 - \left(\frac{\rho_B}{\rho_X}\right) \quad (2)$$

$$d_x = \frac{8M}{Na^3} \quad (3)$$

where M is the molecular weight of the corresponding composition, N is the Avogadro's number (6.026×10^{23} atoms mol^{-1}) and a^3 is the volume of the unit cell.

The average crystal size is 46 nm calculated using the relation (4):

$$G = \frac{K\lambda}{\beta \cos\theta} \quad (4)$$

where $k = 0.9$, λ is the wavelength of X-rays Cu Kα radiation (~1.54 Å), β is the full width half maximum and θ is the angle of the diffraction.

Fig. 2 shows the differential scanning calorimetry (DSC) and thermo-gravimetric analysis (TGA) of $NiTiO_3$. DSC is used to analyze the endothermic and/or exothermic process of the material, and it measures the phase change, purity, evaporation, melting point, crystallization and heat capacity etc. The DSC curve shows the initial endothermic peak at 76.02 °C, the dehydration from 53 °C to 130 °C. An exothermic peak at 309.24 °C is a decomposition of residual organic compounds. A small peak at 400 °C is due to the formation of NiO. A small shoulder around 420 °C indicated the initiation of ordered solid state transitions leading to the formation of $NiTiO_3$. TGA curve shows the decomposition of the materials at three points indicating the weight loss of the material. The first weight loss is due to dehydration of water molecules, and the observed weight loss is 15.13%. The second weight loss has been observed from 100 °C to 320 °C is 34.94%. It has occurred due to decomposition of nickel, titanate and residual organic compounds. The third weight loss 320 °C to 600 °C due to

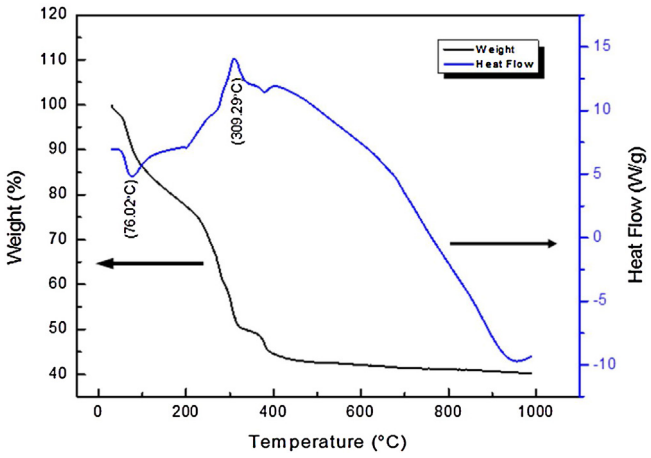

Fig. 2 – TGA and DSC curve of $NiTiO_3$.

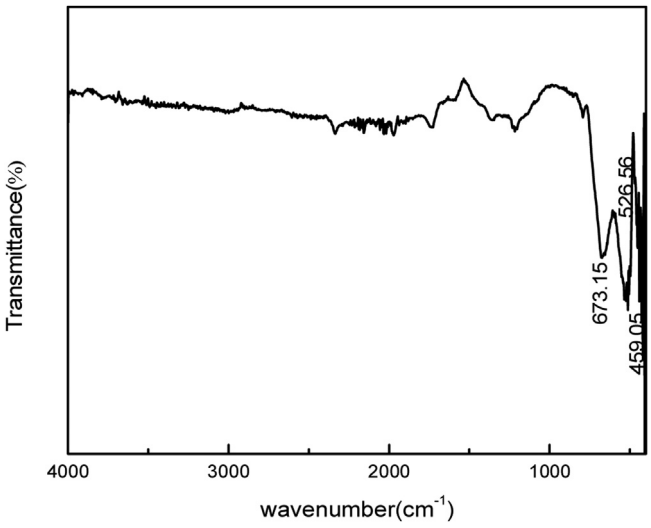

Fig. 3 – FT-IR spectra of NT.

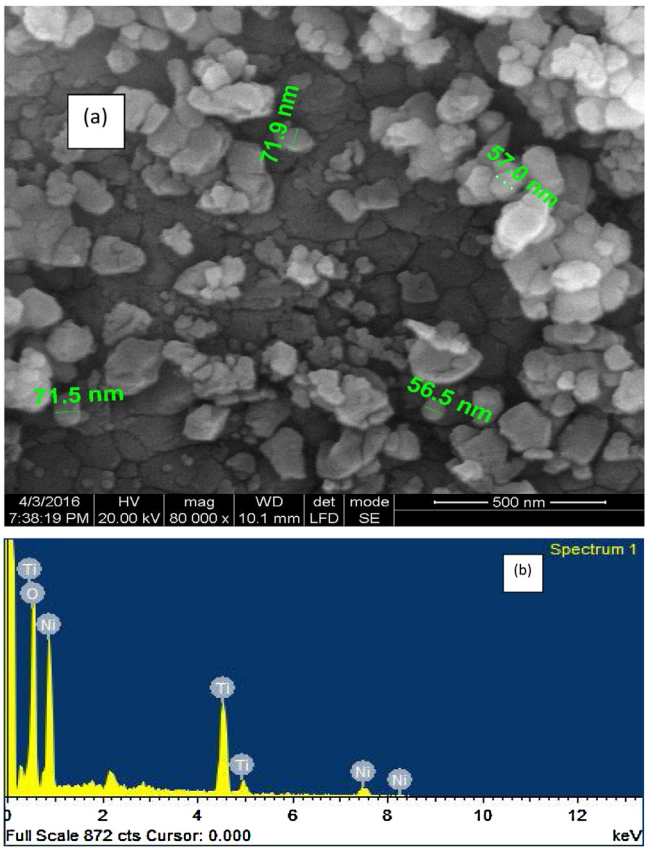

Fig. 4 – (a) HRSEM and (b) EDAX pattern of $NiTiO_3$.

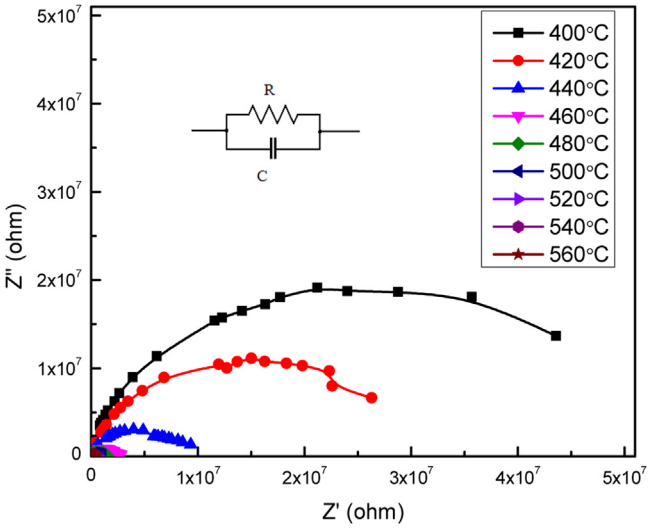

Fig. 5 – Impedance spectra of NT at various temperatures.

degradation of butoxide. Finally, crystallization of $NiTiO_3$ has occurred [6,8,10,17] after 600 °C with no weight loss.

The bond formation in the sample is studied using FT-IR analysis, in the range of 4000–400 cm^{-1}. The characteristic vibration of metal–oxygen bond is supposed to be in the range 700–400 cm^{-1}. Fig. 3 shows the FT-IR spectrum of $NiTiO_3$. The wavelengths of 673.15 cm^{-1} and 526.56 cm^{-1} are stretching vibrations of Ni–O and Ti–O bonds. The sharp absorption peak at 459.05 cm^{-1} confirms the metal titanate bond Ti–O–Ni [5]. Fig. 4(a) and (b) shows the morphology and elemental analysis of $NiTiO_3$. The high-resolution scanning electron microscope (HRSEM) image shows (Fig. 4(a)) uniform grain growth and size distribution of $NiTiO_3$. The particle size is between 56.5 nm and 71.9 nm. The energy dispersive spectrum in Fig. 4(b) shows no impurities in the synthesized $NiTiO_3$.

3.2. *Electrical analysis*

3.2.1. *Impedance analysis*

The complex impedance spectroscopy technique gives an insight into various contributions of the electrical characteristics of the material. The Cole–Cole plot is plotted between the real and imaginary parts of the impedance. The shape of these plots is usually like two semicircles where the semicircle at a lower frequency is electrical contribution due to grain boundaries while the second arises due to grains and occurs at higher frequencies [18]. Fig. 5 shows the Cole–Cole plot of $NiTiO_3$ in 400–500 °C temperature range. Center of the semicircles lies below the *X*-axis called as non-Debye

Table 1 – Conductance parameters from Cole–Cole plot.

Temperature(°C)	R_b(×10^7 ohm)	C_b pF	τ (s)	σ_{dc} (S cm^{-1}) Cole–Cole plot
400	5.0192	6.345	3.184×10^{-4}	5.454×10^{-8}
420	2.9509	7.708	2.274×10^{-4}	9.282×10^{-8}
440	1.0485	5.062	5.307×10^{-5}	2.612×10^{-7}
460	0.2815	5.655	1.592×10^{-5}	9.728×10^{-7}
480	0.1438	5.533	7.961×10^{-6}	1.903×10^{-6}
500	0.1060	5.002	5.307×10^{-6}	2.581×10^{-6}
520	0.0539	5.903	3.184×10^{-6}	5.078×10^{-6}
540	0.0484	3.283	1.592×10^{-6}	5.649×10^{-6}
560	0.0449	3.540	1.592×10^{-6}	6.091×10^{-6}

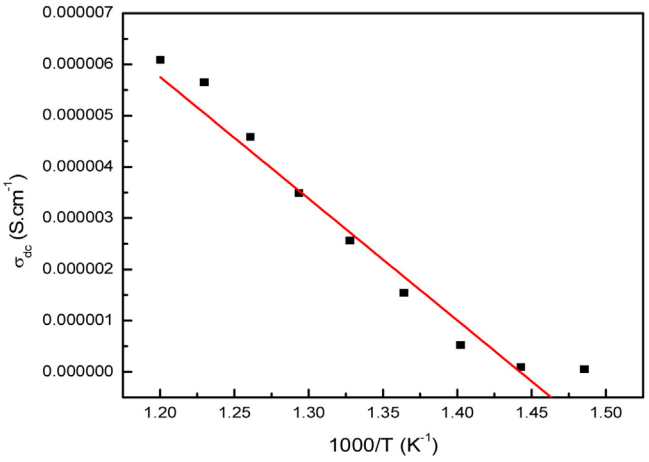

Fig. 6 – Arrhenius plot of $NiTiO_3$.

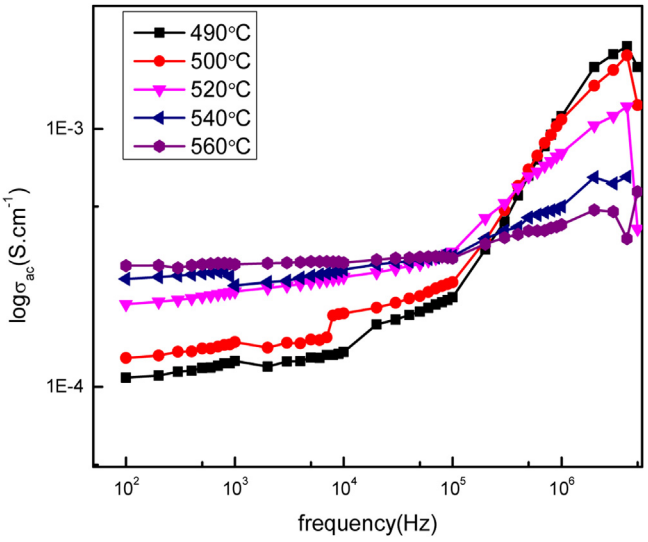

Fig. 7 – Conductance spectra of NT at different temperature.

relaxation. In the plot, it can be noted a single semi-circle is present at higher frequency region. This indicates the intra-grain conduction and no effect of grain boundaries. The relaxation frequency and time at all temperatures can be estimated using the relation:

$$\tau = \frac{1}{\omega} \quad \text{(or)} \quad R_b C_b \tag{5}$$

where $\omega = 2\pi\nu_{max}$, ν_{max} is applied frequency corresponding to the arc maximum. The conduction of the material is calculated using the relation:

$$\sigma_{dc} = \frac{L}{AR_b} \tag{6}$$

where the intercept of the semicircle with *X*-axis gives the bulk resistance R_b (ohm), *L* is the thickness and *A* is the cross-sectional area of the pelletized $NiTiO_3$ sample (in cm), and σ is the conductivity (S cm^{-1}). The inset of Fig. 5 represents the equivalent RC circuit of the bulk conductance of $NiTiO_3$. The value of bulk capacitance is calculated using the relation $2\pi\nu_{max}R_bC_b = 1$ (or) $\omega R_bC_b = 1$. The value of relaxation time can be evaluated using the R_b and C_b values. The calculated values are tabulated in Table 1. It is observed that the relaxation time is decreased with an increase in temperature. It is indicating an increase in the electrical conductivity with increase in temperature. Similar semiconducting behavior is noticed and reported [19,20] in polycrystalline complex titanium ceramics. Fig. 6 shows the variation of σ_{dc} with the inverse of temperature (1000/*T*). The linearity of the plot is associated with thermally activated behavior. The activation energy is found to be 0.041 μeV. Frequency dependence of conductivity is plotted at various temperatures ranging from 490 °C to 560 °C in Fig. 7. At low frequencies, the conductance is steady and low which may be accounted for dc conduction. A linear increase is noticed from 0.1 MHz to 5 MHz, which indicated the dominant role of grains in conduction mechanism than grain boundaries. A small shoulder (kink) noticed at 4 MHz must be due to instrumental error as 5 MHz is the limit of the instrument.

3.3. *Magnetic studies*

The field dependence of magnetic moment in an applied field of ±15 kV at room temperature is shown in Fig. 8. The narrow peak shows the existence of ferromagnetic materials in the sample. At low-temperatures $NiTiO_3$ exhibits antiferromagnetic behavior while ferromagnetic behavior at high temperatures, as reported elsewhere [5]. In the entire range of applied field, $NiTiO_3$ is not saturated. This may be due to high antiferromagnetic interactions at room temperature. The spin interaction between the Ni^{2+}–Ni^{2+} ions is more, so high magnetic field is required to align the spins in the field direction. The coercive field, retentivity and magnetization are 195.72 G, 220.91×10^{-6} emu and 15.994×10^{-3} emu respectively. These

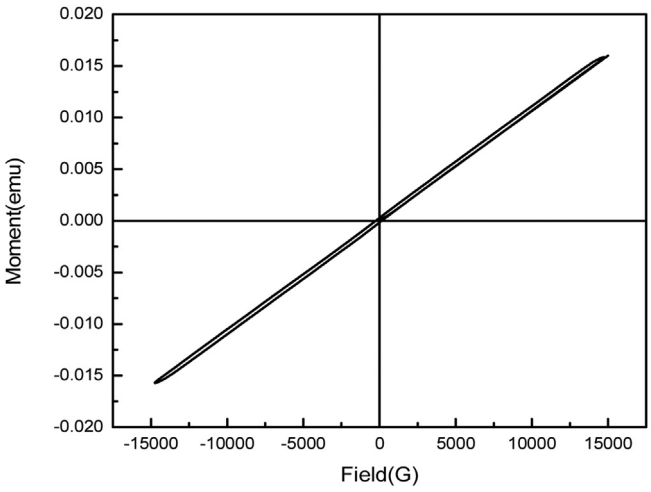

Fig. 8 – M–H loop of $NiTiO_3$.

low values indicate that $NiTiO_3$ is super paramagnetic in nature.

4. Summary and conclusion

In summary, we have obtained with success $NiTiO_3$ nanoparticles synthesized by the sol–gel method and processed in microwaves at 1000 °C for 45 min. X-ray diffractions patterns confirm the rhombohedral phase and dense $NiTiO_3$ formation. Thermal analysis of DSC and TGA is confirms the crystallization stating point at 600 °C. FTIR characterization of $NiTiO_3$ confirms the Ni–O, Ti–O and Ni–O–Ti bond formations and their corresponding vibrational frequencies. HRSEM analysis revealed uniform grain growth with a particle size distribution between 56 nm and 71 nm. EDX spectrum confirms the purity of synthesized $NiTiO_3$. Conductivity studies confirm the semiconducting nature of $NiTiO_3$ and activation energy is estimated to be 0.04 μeV. Magnetometry measurements have revealed superparamagnetic behavior at room temperature.

Conflicts of interest

The authors declare no conflicts of interest..

REFERENCES

[1] Costa AL, Galassi C, Fabbri G, Roncari E, Capiani C. Pyrochlore phase and microstructure development in lead magnesium niobates materials. J Eur Ceram Soc 2001;21:1165–70.
[2] Madhusudan Reddy K, Babita Baruwati M, Jayalakshmi M, Mohan Rao, Manorama SV. S-, N- and C-doped titanium dioxide nanoparticles: synthesis, characterization and redox charge transfer study. J Solid State Chem 2005; 178:3352–8.
[3] Nguyen-Phan T-D, Nguyen-Huy C, Shin EW. Morphological evolution of hierarchical nickel titanates by elevation of the solvothermal temperature. Mater Lett 2014;131:217–21.
[4] Ruiz-Preciado MA, Kassiba A, Gibaud A, Morales-Acevedo A. Comparison of nickel titanate ($NiTiO_3$) powders synthesized by sol–gel and solid state reaction. Mater Sci Semicond Process 2015;37:171–8.
[5] Yuvaraj S, Nithya VD, Saiadali Fathima K, Sanjeeviraja C, Kalai Selvan G, Arumugam S, et al. Investigations on the temperature dependent electrical and magnetic properties of $NiTiO_3$ by molten salt synthesis. Mater Res Bull 2013;48:1110–6.
[6] Lopes KP, Canalcante LS, Simoes AZ, Varela JA, Longo E, Leite ER. $NiTiO_3$ powder obtained by polymeric precursor method: synthesis and characterization. J Alloy Compd 2009;468:327–32.
[7] Taylor DJ, Fleig PF, Page RA. Characterization of nickel titanate synthesized by sol–gel processing. Thin Solid Films 2002;408:104–10.
[8] El-Fattah Gabal MA, Mohamed Al Angari Y, Yousef Obaid A. Structural characterizations and activation energy of $NiTiO_3$ nanopowders prepared by the co-precipitation and impregnation with calcinations. C R Chimie 2013;16:704–11.
[9] Jing P, Lan W, Su Q, Yu M, Xie E. Visible-light photocatalytic activity of novel $NiTiO_3$ nanowires with Rosary-like shape. Sci Adv Mater 2014;6:1–7.
[10] Yang G, Chang W, Yan W. Fabrication and characterization of $NiTiO_3$ nanofibers by sol–gel assisted electrospinning. J Sol–Gel Sci Technol 2014;69:473–9.
[11] Anandan S, Lana-Villarreal T, Wu JJ. Sonochemical synthesis of mesoporous $NiTiO_3$ ilmenite nanorods for the catalytic degradation of tergitol in water. Ind Eng Chem Res 2015;54:2983–90.
[12] Lopes KP, Cavalcante LS, Simoes AZ, Goncalves RF, Escote MT, Varela JA, et al. $NiTiO_3$ nanoparticles encapsulated with SiO_2 prepared by sol–gel method. J Sol–Gel Sci Technol 2008;45:151–5.
[13] Penchal Reddy M, Madhuri W, Balakrishnaiah G, Ramamanohar Reddy N, Siva Kumar KV, Murthy VRK, et al. Microwave sintering of iron deficient Ni–Cu–Zn ferrites for multilayer chip inductors. Curr Appl Phys 2011;11:191–8.
[14] Penchal Reddy M, Madhuri W, Sadhana K, Kim IG, Hui KN, Hui KS, et al. Microwave sintering of nickel ferrite nanoparticles processed via sol–gel method. J Sol–Gel Sci Technol 2014;70:400–4.
[15] Penchal Reddy M, Madhuri W, Ramamanohar Reddy N, Siva Kumar KV, Murthy VRK, Ramakrishna Reddy R. Influence of copper substitution on magnetic and electrical properties of MgCuZn ferrite prepared by microwave sintering method. Mater Sci Eng C 2010;30:1094–9.
[16] Hu Y, Tasi H-L, Huang C-L. Effect of brookite phase on the anatase–rutile transition in titania nanoparticles. J Eur Ceram Soc 2003;23:691–6.
[17] Bacsa J, Eve DJ, Brown ME. The thermal dehydration decomposition of $Ba[Cu(C_2O_4)_2(H_2O)]\cdot 5H_2O$. J Therm Anal 1997;50:33–50.
[18] Badapanda T, Senthil V, Rout SK, Cavalcante LS, Simoes AZ, Sinha TP, et al. Rietveld refinement, microstructure, conductivity and impedance properties of Ba[Zr0.25Ti0.75]O3 ceramic. Curr Appl Phys 2011;11:1282–93.
[19] Das PR, Choudhary RNP, Samantry BK. Diffuse ferroelectric phase transition in Na2Pb2Sm2Ti4Nb4O30 ceramics. Mater Chem Phys 2007;101:228–33.
[20] Suman CK, Prasad K, Choudhary RNP. Complex impedance studies on tungsten–bronze electroceramic: Pb2Bi3LaTi5O18. J Mater Sci 2006;41:369–75.